VIP Real-Time NMR Spectroscopy Very Important Paper

DOI: 10.1002/anie.201309940

Quantitative Analysis of Location- and Sequence-Dependent Deamination by APOBEC3G Using Real-Time NMR Spectroscopy**

*Ayako Furukawa, Kenji Sugase, Ryo Morishita, Takashi Nagata, Tsutomu Kodaki, Akifumi Takaori-Kondo, Akihide Ryo, and Masato Katahira**

Abstract: *The human antiretroviral factor APOBEC3G (A3G) deaminates the newly synthesized minus strand of the human immunodeficiency virus 1 (HIV-1), which results in the abolition of the infectivity of virus-infectivity-factor (Vif)-deficient HIV-1 strains.[1–6] A unique property of A3G is that it deaminates a CCC hot spot that is located close to the 5′ end more effectively than one that is less close to the 5′ end. However, the mechanism of this process is elusive as it includes nonspecific binding of A3G to DNA and sliding of A3G along the DNA strand. Therefore, this process cannot be analyzed by existing methods using the Michaelis–Menten theory. A new real-time NMR method has been developed to examine the nonspecific binding and the sliding processes explicitly, and it was applied to the analysis of the deamination by A3G. As a result, the location-dependent deamination can be explained by a difference in the catalytic rates that depend on the direction of the approach of A3G to the target cytidine. Real-time NMR experiments also showed that A3G deaminates CCCC tandem hotspots with little redundancy, which suggests that A3G efficiently mutates many CCC hotspots that are scattered throughout the HIV-1 genome.*

The enzyme APOBEC3G (A3G) possesses two consensus zinc-finger-type cytidine deaminase motifs (CD1 and CD2),[2] but only CD2 is catalytically active.[7,8] A3G preferably deaminates the third cytidine of a CCC sequence in single-stranded DNA (ssDNA).[9,10] It was reported that A3G nonspecifically binds to ssDNA and slides along ssDNA over 30 nm (69 nucleotides) without directional preference.[11,12] Interestingly, A3G deaminates CCC hot spots in a location-dependent fashion.[10] A 5′ to 3′ gradient of mutations in HIV RNA, which is transcribed from the minus strand DNA, was observed in vivo.[9,13] This would arise from the 3′ to 5′ deamination gradient of minus strand DNA by A3G. Deamination by A3G has been analyzed by various methods, including gel shift assays,[10,14,15] single-molecule fluorescence resonance energy transfer (FRET) spectroscopy,[11] and atomic force microscopy.[12,16] We previously demonstrated that real-time NMR spectroscopy can be utilized to monitor the deamination reaction and revealed that A3G CD2 deaminates the third cytidine of CC<u>C</u> much faster than the second one (C<u>C</u>C).[17] An advantage of real-time NMR spectroscopy over other methods is that it can directly detect a site-specific deamination reaction. Moreover, this method is sensitive to weak interactions because highly concentrated ssDNA (mM order) can be used for the NMR experiment. The real-time NMR method that we used for the analysis of the deamination process has become increasingly popular and has been used by other groups.[18,19]

Our real-time NMR method monitors the intensity change of the H5–H6 total correlation spectroscopy (TOCSY) peak of the third cytidine of CC<u>C</u> in real time. Using this method, we previously analyzed the deamination of a hot spot that solely exists in ssDNA. To gain insight into the mechanism that underlies the location-dependent deamination by A3G, we further developed this NMR method. First, to determine whether real-time NMR spectroscopy provides sufficiently high spectral and time resolution to distinguish the multiple deamination reactions that occur on ssDNA, we monitored the deamination reactions of ssDNA comprising two CCC hot spots (S_{2CCC} in Table 1; see also the Supporting Information). Obviously, the two hot spots were deaminated at different rates by full-length A3G (Figure 1a). Surprisingly, CD2 alone also deaminated the two hot spots in a location-dependent manner, exhibiting higher activity than full-length A3G (Figure 1b). The higher activity of A3G CD2 was previously observed by Chen and co-workers.[14] F-tests showed that the difference between the deamination rates for

[*] Dr. A. Furukawa, Prof. T. Nagata, Prof. T. Kodaki, Prof. M. Katahira
Institute of Advanced Energy, Graduate School of Energy Science
Kyoto University
Gokasho, Uji, Kyoto 611-0011 (Japan)
E-mail: katahira@iae.kyoto-u.ac.jp
Dr. K. Sugase
Bioorganic Research Institute, Suntory Foundation for Life Sciences
1-1-1 Wakayamadai, Shimamoto, Mishima, Osaka 618-8503 (Japan)
Dr. R. Morishita
CellFree Sciences Co., Ltd., Ehime University Venture
Matsuyama, Ehime 790-8577 (Japan)
Prof. A. Takaori-Kondo
Department of Hematology and Oncology
Graduate School of Medicine, Kyoto University
54 Shogoin-Kawaracho, Sakyo-ku, Kyoto 606-8507 (Japan)
Dr. R. Morishita, Prof. A. Ryo
Department of Microbiology
Yokohama City University School of Medicine
3-9 Fukuura, Kanazawa-ku, Yokohama 236-0004 (Japan)

[**] We thank the Ministry of Education, Science, Sports and Culture of Japan for Grants-in Aid for Scientific Research (24121714, 25115507, and 25291013 to M.K.; 23570146 and 24113710 to T.N.), Japan Science and Technology (CREST; M.K.), the Sumitomo–Denko and Iwatani Foundations (M.K.), and the Japan Society for the Promotion of Science (A.F.). For funding for open access charges, we are grateful to the Ministry of Education, Science, Sports and Culture of Japan (24121714).

Supporting information for this article is available on the WWW under http://dx.doi.org/10.1002/anie.201309940.

Table 1: Oligonucleotides used in this study.

Name	Sequence
S_{2CCC}	ATTCCCAATTTTTTTTATACCCATTT
$S_{CCCssCCC}$	ATTCCCAATTTTTTTTTTTTTTTTTATACCCAT$_{23}$
$S_{CCCdsCCC}$	ATTCCCAATTCGCGAACGCGCAAGCGCATACCCAT$_{23}$ GCGCTTGCGCGTTCGCG
$S_{5'CCC}$	TTACCCAT$_{42}$
S_{mCCC}	T$_{21}$ACCCAT$_{22}$
$S_{3'CCC}$	T$_{41}$ACCCATTT
S_{CCCC}	ATTCCCCATT
S_{CCCU}	ATTCCCUATT
S_{CCUC}	ATTCCUCATT
S_{CCCA}	ATTCCCAATT
S_{CCUA}	ATTCCUAATT
S_{CCUU}	ATTCCUUATT

The cytidines that are to be deaminated are underlined.

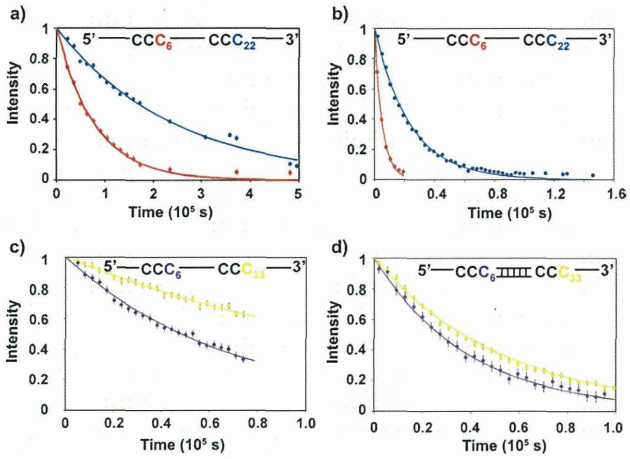

Figure 1. Real-time monitoring of deamination reactions at two CCC hot spots in ssDNA. a, b) Deamination reactions with full-length A3G (a) and CD2 (b) were monitored for C6 (●) and C22 (●) in S_{2CCC}. The deamination rates for full-length A3G are $1.3\times10^{-5}\pm4.0\times10^{-7}$ s^{-1} for C6 and $4.1\times10^{-6}\pm7.4\times10^{-8}$ s^{-1} for C22, and those for CD2 are $2.0\times10^{-4}\pm7.5\times10^{-6}$ s^{-1} for C6 and $4.2\times10^{-5}\pm5.0\times10^{-7}$ s^{-1} for C22. c, d) Deamination reactions of CD2 were monitored for C6 (●) and C33 (●) in $S_{CCCssCCC}$ (c) and $S_{CCCdsCCC}$ (d).

the two hot spots is statistically significant for both full-length A3G and CD2. The same result was obtained with ssDNA in which two units of S_{2CCC}, ATTCCCAAT and ATACCCATT, had swapped positions. These results confirmed that CD2 alone causes the location-dependent deamination. Although catalytically inactive CD1 also supposedly contributes to the location-dependent deamination process, we assumed that the intrinsic characteristics of CD2 are important for the location-dependent deamination by full-length A3G. We focused on CD2 in the following experiments. Subsequently, we investigated whether our real-time NMR method can be used to examine the sliding of A3G along ssDNA. As A3G binds to ssDNA, but not to dsDNA,[10] intervening dsDNA should block the sliding of A3G. As shown in Figure 1c and d, the deamination rates of two hot spots in a substrate with short dsDNA between them were almost the same, whereas the rates were location-dependent without dsDNA ($S_{CCCdsCCC}$ and $S_{CCCssCCC}$ in Table 1). This finding clearly indicates that real-time NMR spectroscopy can sense the sliding of A3G CD2 along ssDNA.

We have thus confirmed that real-time NMR spectroscopy is sufficiently sensitive to location-dependent deamination reactions and sliding processes of A3G CD2. Based on these results, we designed experiments and constructed a kinetic model to quantitatively analyze the deamination reaction. As A3G binds to ssDNA nonspecifically, the binding rate should depend on the length of the ssDNA and the concentrations of A3G and ssDNA. On the other hand, the duration of the sliding to reach a hot spot should depend on the length of the ssDNA and the position of a hot spot. Therefore, the kinetics of the deamination reaction can be determined by real-time NMR studies with different concentrations of ssDNA and A3G CD2, and with ssDNAs of different lengths and with different positions of hot spots. According to this idea, we developed a kinetic model for the analysis of real-time NMR data (see the Supporting Information). The deamination reaction that is monitored by NMR spectroscopy as a change of intensity, $I(t)$, is expressed as:

$$I(t) = I_0\exp(-k_{deami}t) \quad (1)$$

I_0 is the initial intensity, which is proportional to the concentration of ssDNA, and k_{deami} represents the apparent deamination rate, which is calculated as detailed below:

$$k_{deami} = \frac{[^NS][^NE]}{S_0K_d}\{k_{cat(3'\to5')}(1-\alpha^n) + k_{cat(5'\to3')}(1-\alpha^{N-n+1})\} \quad (2)$$

$$[^NS] = \frac{1}{2}\left(-{}^N\beta + S_0 - E_0 + \sqrt{({}^N\beta - S_0 + E_0)^2 + 4E_0{}^N\beta}\right) \quad (3)$$

$$[^NE] = \frac{1}{2}\left(-{}^N\beta - S_0 + E_0 + \sqrt{({}^N\beta + S_0 - E_0)^2 + 4E_0{}^N\beta}\right) \quad (4)$$

$$\alpha = k_s/(k_s + k_{off}), \quad {}^N\beta = \frac{K_d}{2\{N+1-(1-\alpha^{N+1})/(1-\alpha)\}} \quad (5)$$

N and n represent the total number of nucleotides in ssDNA and the position of the reacting cytidine from the 3' end, respectively. According to this kinetic model, A3G CD2 binds to any nucleotide of ssDNA with an association rate constant k_{on} and dissociates from ssDNA with a dissociation rate constant k_{off}. A3G CD2 slides along ssDNA in both directions at a sliding rate k_s (Figure 2a). As the ssDNAs used are relatively short (49–57 nucleotides), we assumed that the sliding of A3G CD2 does not change direction during a single sliding event. The structure of the A3G–ssDNA complex has not been determined yet; therefore, it is still unknown how A3G recognizes a hot spot. On the other hand, the structure of free A3G CD2 has already been determined, and a protruding bump that hangs over one side of the catalytic pocket, which includes the catalytic residue Glu259 and the zinc ion, was revealed (Supporting Information, Figure S1a).[14,17,20] We assumed that this bump interferes with the accommodation of the target cytidine into the catalytic pocket; this process depends on the direction of the approach of A3G CD2 (Figure S1b,c). Then, we incorporated two cata-

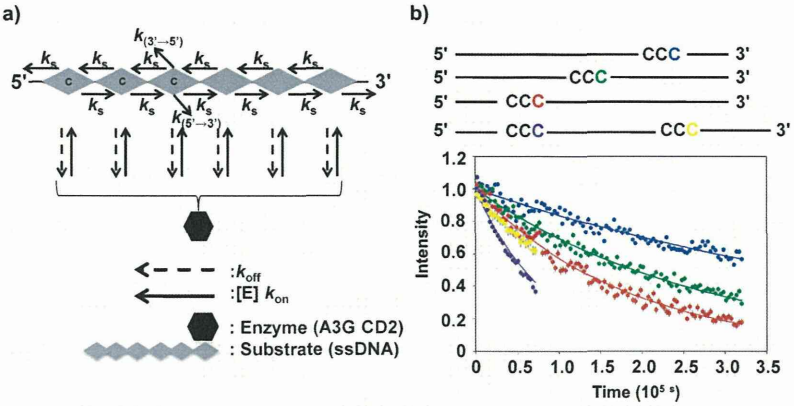

Figure 2. Quantitative analysis of the location-dependent deamination reaction using real-time NMR spectroscopy. a) Kinetic model of the deamination reaction by A3G. b) Real-time NMR data for C6 of $S_{5'CCC}$ (●), C26 of S_{mCCC} (●), C45 of $S_{3'CCC}$ (●), and both C6 (●) and C33 (●) of $S_{CCCssCCC}$ were fitted to Eq. (1).

lytic rates, $k_{cat(3'\rightarrow5')}$ and $k_{cat(5'\rightarrow3')}$, into the model, which are the catalytic rates for the cases where A3G CD2 approaches the target cytidine from downstream and upstream, respectively. As A3G slides along ssDNA without directional preference,[12] the location-dependent deamination is difficult to explain without the two different k_{cat} values. These k_{cat} values represent the rates of the entry of ssDNA into the catalytic pocket and of its deamination. A global fit of multiple real-time NMR data collected under different conditions (see above) provided the parameters α, K_d ($=k_{off}/k_{on}$), $k_{cat(3'\rightarrow5')}$, and $k_{cat(5'\rightarrow3')}$. However, it is difficult to separate α into k_s and k_{off} because neither the sliding nor the dissociation process can be perturbed experimentally without affecting the other process. The NMR data were fitted to Eq. (1) using the program GLOVE.[21]

For this analysis, we obtained real-time NMR data for $S_{5'CCC}$, S_{mCCC}, and $S_{3'CCC}$ (Table 1) aside from the data for the aforementioned two hot spots of $S_{CCCssCCC}$. These data are in good agreement with Eq. (1), yielding values for $k_{cat(3'\rightarrow5')}$ and $k_{cat(5'\rightarrow3')}$ of 68 s^{-1} and 14 s^{-1}, respectively (Figure 2b). The closer a CCC hot spot is located to the 5′ end, the more chance it has of being detected by A3G approaching from downstream rather than from upstream; therefore, a CCC hot spot that is located close to the 5′ end is deaminated more rapidly than one that is less close to the 5′ end.

For further applications of our real-time NMR method, we analyzed the deamination of CCCC, in which two CCC sequences overlap (S_{CCCC} in Table 1). The clusters of three to six consecutive cytidines are scattered throughout the HIV genome, and CCCC is the second most abundant cluster after CCC. Unfortunately, the NMR peaks that need to be monitored during the deamination reactions overlapped, for example, the TOCSY peaks of the fourth cytidines of CCCC and CCUC. Therefore, the time courses of each deamination reaction could not be monitored separately (Figure 3a and b). However, the results of the deamination reactions were characterized using the NMR spectrum of the same ssDNA whose deamination reactions had reached completion. As a result, the third and fourth cytidines of CCCC were found to be deaminated by A3G CD2 with equal efficiency because the intensities of peaks 2 (CCUC) and 3 (CCCU + CCUU) were nearly identical. This finding is different from that of a previous study with a gel shift assay; in the earlier case, the third cytidine was deaminated more efficiently than the fourth cytidine.[15] This discrepancy could be due to the difference in the duration of the monitoring between our NMR method (6 h) and the gel shift assay (3 min). Real-time NMR spectroscopy can monitor multiple reactions directly and simultaneously using a single sample, whereas the gel shift assay cannot. Therefore, our results should provide more accurate information.

The deamination of CCCU into CCUU is redundant and may be unnecessary for abolition of the HIV infectivity. However, the above experiment could not provide information on the deamination efficiency for CCCU because the NMR peaks of CCUU and CCUC overlapped. Thus, we monitored the deamination reactions for CCCA (non-deaminated site) and CCCU (monodeaminated site) to determine whether or not A3G has a preference for either of the two sequences, S_{CCCA} and S_{CCCU} (Table 1). In this case, the deamination reactions were monitored by one-dimensional ^{1}H NMR spectroscopy to increase spectral resolution (Figure 3c and d). The results revealed that A3G preferentially deaminates a non-deaminated site rather than a monodeami-

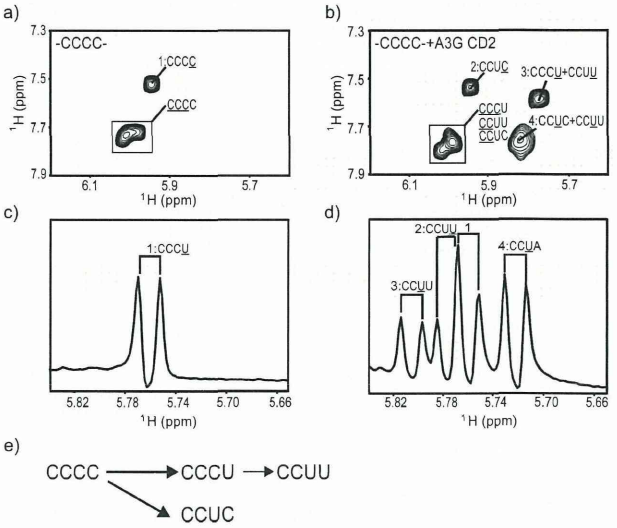

Figure 3. Deamination reactions of CCCC by A3G CD2. a, b) TOCSY spectrum of S_{CCCC} (a) and TOCSY spectrum recorded six hours after the addition of A3G CD2 (b). The peaks are labeled with the sequences of the corresponding substrates or deaminated products in which the assigned residues are underlined (see the Supporting Information). c, d) ^{1}H NMR spectrum of an equimolar mixture of S_{CCCA} and S_{CCCU} (c), and ^{1}H NMR spectrum recorded 40 minutes after the addition of A3G CD2 (d). Peaks 1 to 4 were assigned by recording the NMR spectra of S_{CCUU} and S_{CCUA}. e) Two possible deamination reaction pathways for CCCC.

nated site because the intensity of the peak for the deaminated product CCUA (peak 4) was greater than that of the peak corresponding to CCUU (peak 3). A3G would exploit this sequential preference to efficiently deaminate multiple hot spots that are scattered throughout the HIV genome with a small amount of redundant deamination of CCCC.

In conclusion, we analyzed real-time NMR data for the location-dependent deamination by A3G CD2 using a newly derived kinetic model. As a result, the location-dependent deamination can be explained by the difference in the rate constants k_{cat} of CD2, which depend on the direction of the approach to the target cytidine. We also characterized deamination reactions of CCCC by real-time NMR spectroscopy, even though multiple reactions occurred simultaneously. Previously, it was proposed that the location-dependent deamination is caused by two binding orientations on ssDNA and the existence of a region where either less or no deamination occurs (ca. 30 nucleotides) at the 3′ end of the ssDNA.[10,16] However, this model cannot explain the location-dependent deamination that is observed for long ssDNA (70 nucleotides)[15] because the contribution of the dead region to the location dependency becomes smaller. On the other hand, our model can explain the location-dependent deamination reaction even for such a long ssDNA fragment.

Recently, it was proposed that the proteins of the APOBEC family are involved in epigenesis.[22] They may contribute to the removal of an epigenetic marker, a methyl group of a 5-methyl cytosine, through deamination of 5-hydroxymethyl cytosine. Our real-time NMR method could also be applied to examine such DNA modifications and to provide insight into epigenesis. Furthermore, this method can also be used for the analysis of post-translation modifications of proteins.

Received: November 15, 2013
Published online: January 29, 2014

Keywords: deamination · DNA · enzyme kinetics · quantitative analysis · NMR spectroscopy

[1] A. M. Sheehy, N. C. Gaddis, J. D. Choi, M. H. Malim, *Nature* **2002**, *418*, 646–650.
[2] R. S. Harris, M. T. Liddament, *Nat. Rev. Immunol.* **2004**, *4*, 868–877.
[3] D. Lecossier, F. Bouchonnet, F. Clavel, A. J. Hance, *Science* **2003**, *300*, 1112.
[4] B. Mangeat, P. Turelli, G. Caron, M. Friedli, L. Perrin, D. Trono, *Nature* **2003**, *424*, 99–103.
[5] H. Zhang, B. Yang, R. J. Pomerantz, C. Zhang, S. C. Arunachalam, L. Gao, *Nature* **2003**, *424*, 94–98.
[6] R. S. Harris, K. N. Bishop, A. M. Sheehy, H. M. Craig, S. K. Petersen-Mahrt, I. N. Watt, M. S. Neuberger, M. H. Malim, *Cell* **2003**, *113*, 803–809.
[7] G. Hache, M. T. Liddament, R. S. Harris, *J. Biol. Chem.* **2005**, *280*, 10920–10924.
[8] F. Navarro, B. Bollman, H. Chen, R. Konig, Q. Yu, K. Chiles, N. R. Landau, *Virology* **2005**, *333*, 374–386.
[9] Q. Yu, R. Konig, S. Pillai, K. Chiles, M. Kearney, S. Palmer, D. Richman, J. M. Coffin, N. R. Landau, *Nat. Struct. Mol. Biol.* **2004**, *11*, 435–442.
[10] L. Chelico, P. Pham, P. Calabrese, M. F. Goodman, *Nat. Struct. Mol. Biol.* **2006**, *13*, 392–399.
[11] L. S. Shlyakhtenko, A. Y. Lushnikov, A. Miyagi, M. Li, R. S. Harris, Y. L. Lyubchenko, *Biochemistry* **2012**, *51*, 6432–6440.
[12] G. Senavirathne, M. Jaszczur, P. A. Auerbach, T. G. Upton, L. Chelico, M. F. Goodman, D. Rueda, *J. Biol. Chem.* **2012**, *287*, 15826–15835.
[13] R. Suspène, C. Rusniok, J. P. Vartanian, S. Wain-Hobson, *Nucleic Acids Res.* **2006**, *34*, 4677–4684.
[14] L. G. Holden, C. Prochnow, Y. P. Chang, R. Bransteitter, L. Chelico, U. Sen, R. C. Stevens, M. F. Goodman, X. S. Chen, *Nature* **2008**, *456*, 121–124.
[15] R. Nowarski, E. Britan-Rosich, T. Shiloach, M. Kotler, *Nat. Struct. Mol. Biol.* **2008**, *15*, 1059–1066.
[16] L. Chelico, C. Prochnow, D. A. Erie, X. S. Chen, M. F. Goodman, *J. Biol. Chem.* **2010**, *285*, 16195–16205.
[17] A. Furukawa, T. Nagata, A. Matsugami, Y. Habu, R. Sugiyama, F. Hayashi, N. Kobayashi, S. Yokoyama, H. Takaku, M. Katahira, *EMBO J.* **2009**, *28*, 440–451.
[18] S. Harjes, W. C. Solomon, M. Li, K. M. Chen, E. Harjes, R. S. Harris, H. Matsuo, *J. Virol.* **2013**, *87*, 7008–7014.
[19] I. J. Byeon, J. Ahn, M. Mitra, C. H. Byeon, K. Hercik, J. Hritz, L. M. Charlton, J. G. Levin, A. M. Gronenborn, *Nat. Commun.* **2013**, *4*, 1890.
[20] K. M. Chen, E. Harjes, P. J. Gross, A. Fahmy, Y. Lu, K. Shindo, R. S. Harris, H. Matsuo, *Nature* **2008**, *452*, 116–119.
[21] K. Sugase, T. Konuma, J. C. Lansing, P. E. Wright, *J. Biomol. NMR* **2013**, *56*, 275–283.
[22] N. Bhutani, D. M. Burns, H. M. Blau, *Cell* **2011**, *146*, 866–872.

EUROPEAN JOURNAL OF Haematology

European Journal of Haematology 92 (219–228)

ORIGINAL ARTICLE

Antitumor effects of bevacizumab in a microenvironment-dependent human adult T-cell leukemia/lymphoma mouse model

Fumiko Mori[1], Takashi Ishida[1], Asahi Ito[1], Fumihiko Sato[2], Ayako Masaki[1], Tomoko Narita[1], Susumu Suzuki[2], Tomiko Yamada[1], Hisashi Takino[2], Masaki Ri[1], Shigeru Kusumoto[1], Hirokazu Komatsu[1], Masakatsu Hishizawa[3], Kazunori Imada[4], Akifumi Takaori-Kondo[3], Akio Niimi[1], Ryuzo Ueda[5], Hiroshi Inagaki[2], Shinsuke Iida[1]

[1]Department of Medical Oncology and Immunology, Nagoya City University Graduate School of Medical Sciences, Nagoya;[2]Department of Anatomic Pathology and Molecular Diagnostics, Nagoya City University Graduate School of Medical Sciences, Nagoya; [3]Department of Hematology and Oncology, Graduate School of Medicine, Kyoto University, Kyoto; [4]Department of Hematology, Kokura Memorial Hospital, Kitakyushu; [5]Department of Tumor Immunology, Aichi Medical University School of Medicine, Nagakute, Japan

Abstract

Objective: The objective of this study was to evaluate the therapeutic potential of bevacizumab with or without systemic chemotherapy for adult T-cell leukemia/lymphoma (ATL) and clarify the significance of angiogenesis for ATL pathogenesis. *Methods:* NOD/Shi-*scid*, IL-2Rγ^{null} (NOG) mice were used as recipients of tumor cells from a patient with ATL, which engraft and proliferate in a microenvironment-dependent manner. The ATL cells could be serially transplanted in NOG mice, but could not be maintained in *in vitro* cultures. *Results:* Injection of bevacizumab alone significantly increased necrosis and decreased vascularization in the tumor tissue. Levels of human soluble interleukin two receptor in the serum (reflecting the ATL tumor burden) of bevacizumab-treated mice were significantly lower than in untreated mice. Although bevacizumab monotherapy showed these clear anti-angiogenesis effects, it did not prolong survival. In contrast, injection of bevacizumab together with cyclophosphamide, doxorubicin, vincristine, prednisolone (CHOP) led to a significant prolongation of survival of the ATL mice relative to CHOP alone. *Conclusions:* This is the first report to evaluate the efficacy of bevacizumab for ATL in a tumor microenvironment-dependent model. Bevacizumab therapy combined with chemotherapy could be a valuable treatment strategy for that subgroup of ATL probably depending to a large extent on angiogenesis via vascular endothelial growth factor.

Key words Adult T-cell leukemia-lymphoma; Bevacizumab; tumor microenvironment

Correspondence Takashi Ishida, MD, PhD, Department of Medical Oncology and Immunology, Nagoya City University Graduate School of Medical Sciences, 1 Kawasumi, Mizuho-chou, Mizuho-ku, Nagoya, Aichi 467-8601, Japan. Tel: +81 52 853 8216; Fax: +81 52 852 0849; e-mail: itakashi@med.nagoya-cu.ac.jp

Accepted for publication 29 October 2013

doi:10.1111/ejh.12231

Adult T-cell leukemia-lymphoma (ATL) is an aggressive peripheral T-cell neoplasm caused by human T-cell lymphotropic virus type 1 (HTLV-1). The disease is resistant to conventional chemotherapeutic agents, and currently there are only limited treatment options; thus, it has a very poor prognosis (1–4). Over the past decade, allogeneic hematopoietic stem-cell transplantation has evolved into a potential approach to treating patients with ATL. However, only a small fraction of patients have the opportunity to benefit from transplantation, such as those who are younger, have achieved sufficient disease control, and have an appropriate stem-cell source (5, 6). Therefore, the development of alternative treatment strategies for patients with ATL is an urgent issue.

Bevacizumab is a humanized monoclonal antibody against the vascular endothelial growth factor A (VEGF-A), a key

factor inducing the formation of blood vessels (angiogenesis) in tumors (7). Bevacizumab is currently approved worldwide for the treatment of several types of cancer such as metastatic colorectal cancer, metastatic non-small-cell lung cancer, renal cell carcinoma, and advanced ovarian cancer, in combination with chemotherapy or interferon (8–14). Bevacizumab is also approved as a single agent for recurrent glioblastoma in the USA (15). In this context, many aspects of pathological angiogenesis have been extensively studied in many types of cancer. On the other hand, the precise role of these processes in pathogenesis of hematological malignancies including ATL is still under active investigation (16–19). Thus far, bevacizumab has not been approved for the treatment of any hematological malignancy in the USA, Europe, or Japan. The aim of the present study was to evaluate the therapeutic potential of bevacizumab with or without systemic chemotherapy for ATL and clarify the significance of angiogenesis for ATL pathogenesis, using a microenvironment-dependent murine ATL model.

Methods

Animals

NOD/Shi-*scid*, IL-2Rγ^{null} (NOG) mice (20) were purchased from the Central Institute for Experimental Animals (Kanagawa, Japan) and used at 6–8 wk of age. All of the *in vivo* experiments were performed in accordance with the United Kingdom Coordinating Committee on Cancer Research Guidelines for the Welfare of Animals in Experimental Neoplasia, Second Edition, and were approved by the Ethics Committee of the Center for Experimental Animal Science, Nagoya City University Graduate School of Medical Sciences.

Immunopathological analysis

We assessed the affected lymph nodes of 23 patients with ATL by immunopathology. The patients provided written informed consent in accordance with the Declaration of Helsinki, and this present study was approved by the institutional Ethics Committee of Nagoya City University Graduate School of Medical Sciences. Hematoxylin and eosin (HE) staining and immunostaining using anti-human CD4 (4B12; Novocastra, Wetzlar, Germany), CD25 (4C9; Novocastra), CD20 (L26; DAKO, Glostrup, Denmark), VEGF-A (sc-152, rabbit polyclonal; Santa Cruz, Heidelberg, Germany), Alpha-Smooth Muscle Actin (α-SMA) (1A4; DAKO), CD31 (JC70A; DAKO), and von Willebrand Factor (Rabbit polyclonal; DAKO) were performed on formalin-fixed, paraffin-embedded sections. VEGF-A expression levels were categorized according to the following formula: 3+ positive if ≥50%, 2+ positive if <50 ≥30%, 1+ positive if <30 ≥10%, and negative if <10% of the ATL tumor cells were stained with the corresponding antibody. Nine 100× high-power fields (HPF) of HE tumor specimens were randomly selected, and the area of tumor necrosis (%) was calculated by Image J software (21), and then averaged. Nine 100× HPF of von Willebrand Factor-stained tumor specimens were randomly selected, and numbers of vessels (per mm^2) were calculated by Image J software and then averaged.

ATL mouse model

A leukemic cell clone from a patient with ATL, which could be serially transplanted into SCID mice, designated S-YU as reported previously (22), was injected intraperitoneally (i.p.) into NOG mice. Three to 4 wk after i.p. injection, NOG mice were presented with intraperitoneal masses along the mesentery. Cells from these intraperitoneal masses were suspended in RPMI-1640 and inoculated i.p. into healthy NOG mice, which then presented with features identical to those of the original mice.

Cell lines

ATN-1, MT-1, and TL-Om1 are ATL cell lines, whereas MT-2, MT-4, and TL-Su are HTLV-1-immortalized lines, as previously described (23).

Quantitative reverse transcription-polymerase chain reaction

Total RNA was isolated with RNeasy Mini Kits (QIAGEN, Tokyo, Japan). Reverse transcription from the RNA to first strand cDNA was carried out using High Capacity RNA-to-cDNA Kits (Applied Biosystems Inc, Foster City, CA, USA). *Human VEGF-A* (Hs00900055_m1), *VEGF-R1* (Hs00176573_m1), *VEGF-R2* (Hs00911700_m1), and *β-actin* (Hs99999903_m1) *mRNA* were amplified using TaqMan® Gene Expression Assays with the aid of an Applied Biosystems StepOnePlus™. The quantitative assessment of the mRNA of interest was done by dividing its level by that of *β-actin* and expressing the result relative to Human Testis Total RNA (Clontech, Mountain View, CA, USA) as 1.0. All expressed values were averages of triplicate experiments.

Monoclonal antibodies and flow cytometry

The following Monoclonal antibodies (mAbs) were used for flow cytometry: APC-conjugated anti-human CD45 mAb (2D1; BD Biosciences, San Jose, CA, USA), PerCP-conjugated anti-CD4 mAb (SK3; BD Biosciences), PE-conjugated anti-CD25 mAb (M-A251; BD Biosciences), PE-conjugated VEGF-R1 mAb (49560; BD Biosciences), PE-conjugated VEGF-R2 mAb (89106, R&D Systems, Inc. Minneapolis, MN,

USA), and the appropriate isotype control mAbs. Whole blood was treated with BD FACS lysing solution (BD Biosciences) to remove RBC. Stained cells were analyzed on a FACSCalibur (BD Biosciences) with the aid of FlowJo software (Tree Star, Inc. Ashland, OR, USA).

Cell proliferation assay

Proliferation of S-YU and HTLV-I-immortalized lines expressing both VEGF-A and VEGF-R1 in the presence of different concentrations of bevacizumab for 48 h was assessed using CellTiter 96 Aqueous One Solution cell proliferation assay kits (Promega Corporation, Madison, WI, USA). Bevacizumab was purchased from Chugai Pharmaceutical Co., Ltd., Tokyo, Japan.

ATL cell-bearing mice treated with bevacizumab

ATL tumor cells (S-YU) from the intraperitoneal masses were suspended in RPMI-1640, and 1.0×10^7 was inoculated i.p. into each of 14 NOG mice. The animals were divided into two groups of seven each for treatment with bevacizumab or to serve as controls. Bevacizumab (10 mg/kg) or vehicle (saline) was i.p. injected into the mice 3, 10, and 17 d after tumor cell inoculations. Therapeutic efficacies were evaluated for area of tumor necrosis, number of vessels, and serum human sIL2R levels 22 d after tumor inoculation. The concentration of human sIL2R in the serum was measured by ELISA using human sIL2R immunoassay kits (R&D Systems, Inc.).

ATL cells from the intraperitoneal masses suspended in RPMI-1640 were also inoculated i.p. into another 10 NOG mice at 1.0×10^7 per mouse. These animals were randomly divided into two groups of five each for treatment with bevacizumab or as controls. Bevacizumab (10 mg/kg) or saline was injected i.p. into the mice 2, 9, 16, and 23 d after tumor cell inoculation. Therapeutic efficacy of bevacizumab was evaluated by survival times.

A further 16 NOG mice that had also received 1.0×10^7 ATL cells from intraperitoneal masses were randomly divided into two groups of eight each for treatment with bevacizumab + cyclophosphamide, doxorubicin, vincristine, prednisolone (CHOP) or CHOP alone. Bevacizumab (10 mg/kg) or saline was i.p. injected into the mice 2, 9, 16, 23, 30, and 37 d after tumor cell inoculations. CHOP was given i.p. 17 d after tumor inoculation at the following doses: cyclophosphamide, 40 mg/kg; doxorubicin, 3.3 mg/kg; vincristine, 0.5 mg/kg; and prednisolone, 0.2 mg/kg (24, 25). Therapeutic efficacy of bevacizumab was evaluated by survival time. Cyclophosphamide and vincristine were purchased from Shionogi Pharmaceutical Co., Ltd, Osaka, Japan; doxorubicin was from Kyowa Hakko Kirin Co., Ltd, Tokyo, Japan, and prednisolone was from Nippon Kayaku Co., Ltd, Tokyo, Japan.

Statistical analysis

The differences between groups regarding the tumor necrosis area, vascular number, and human sIL2R concentrations in serum were analyzed by the Mann–Whitney U test. In this study, $P < 0.05$ was considered significant.

Results

VEGF-A expression in ATL

VEGF-A expression by ATL cells in the lymph node lesions is shown in Fig. 1A. Immunopathological features of four cases from each group stratified by VEGF-A expression are shown in Fig. 1B. Most of the ATL cases (96%) were positive for VEGF-A.

ATL cell-bearing NOG mice

In earlier studies, S-YU ATL tumor cells, which were serially transplanted into SCID mice (22), manifested multiple enlarged mesenteric lymph nodes. In the present study, in which NOG mice rather than SCID mice were the S-YU recipients, larger tumor masses formed along the intestinal tract. Figure 2A shows the intraperitoneal masses and intestinal tract adhering tightly to one another in a NOG mouse (demarcated by thin white dotted lines in the figure). Flow cytometric analysis demonstrated that the mass mainly consisted of human cells expressing CD4 and CD25 (Fig. 2B). Immunopathological analysis revealed large atypical cells with irregular and pleomorphic nuclei, and blood vessels. The cells were CD4-positive, CD25-positive, but CD20-negative (Fig. 2C). These findings are consistent with an ATL cell phenotype in humans, and with earlier studies in the SCID/S-YU model. The S-YU tumor cells in the NOG mice were classed as VEGF-A 1+ positive (Fig. 2C). Blood vessels in the tumor tissue were stained by anti-α-SMA Ab (Fig. 2C). Vascular endothelial cells in the tumor tissue were stained by anti-von Willebrand Factor Ab, but not by anti-CD31 mAb (data not shown). Together, these results show that the blood vessels in the tumor tissue originated from the mouse, because anti-α-SMA and von Willebrand Factor Ab used in this study recognized the corresponding protein derived from both human and mouse, whereas the anti-CD31 mAb recognized the corresponding human but not murine protein (data not shown). CD4-positive CD25-positive ATL cell mild infiltration into spleen, liver, and bone marrow was seen by flow cytometry (Fig. 2D).

VEGF-A, VEGF-R1, and -R2 expression in ATL and HTLV-1-immortalized lines

VEGF-A mRNA expression was detected in all 7 ATL and HTLV-1-immortalized lines tested, and in S-YU cells

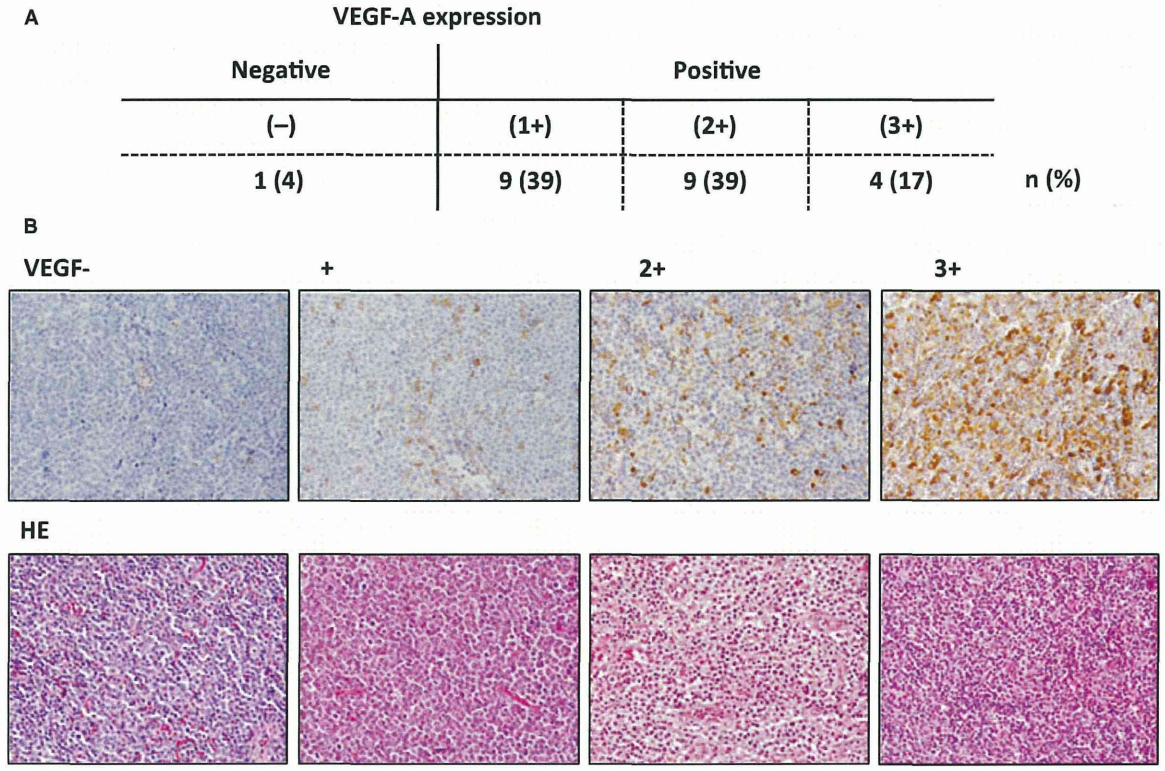

Figure 1 Vascular endothelial growth factor A (VEGF-A) expression in ATL. (A) VEGF-A expression of ATL cells in the lymph node lesion. VEGF-A expression was categorized based on the percentage of ATL cells stained as follows: ≥50%, 3+ positive; 30–49%, 2+ positive; 10–29%, 1+ positive; <10%, negative. (B) Cases 1, 2, 3, and 4 are representative of VEGF-A-negative, 1+, 2+, and 3+ positive categories, respectively. Photomicrographs with VEGF-A (upper panels) and hematoxylin and eosin staining (lower panels) are shown.

from intraperitoneal masses (Fig. 3A, upper left panel). *VEGF-R1 mRNA* expression was not present in ATL and in only two HTLV-1-immortalized lines (MT-2 and TL-Su) but was present in S-YU cells (Fig. 3A, upper right panel). No *VEGF-R2 mRNA* expression was detected in any of the 7 ATL and HTLV-1-immortalized lines tested, or in S-YU cells (data not shown). Flow cytometry demonstrated that VEGF-R1 protein was also expressed in MT-2 and TL-Su, and very weakly in NOG S-YU cells (Fig. 3A, lower panels), consistent with the RT-PCR results. Flow cytometry demonstrated that VEGF-R2 was not expressed at all in any of the ATL and HTLV-1-immortalized lines tested, or in S-YU cells (data not shown), which was also consistent with the RT-PCR results.

VEGF-R1 and VEGF-R2 expression in primary ATL cells

CD4-positive CD25-positive primary ATL cells in PBMC obtained from nine individual patients with ATL (i–ix) were evaluated for VEGF-R1 and -R2 expression. VEGF-R1 protein was expressed in only one patient (patient v) and VEGF-R2 was not expressed in any of the patients (Fig. 4B).

No Bevacizumab-mediated anti-proliferative activity against HTLV-1-immortalized lines and S-YU *in vitro*

Bevacizumab did not directly block the proliferation of MT-2 and TL-Su cells *in vitro*, despite their expression of both VEGF-A and VEGF-R1. Neither did it inhibit S-YU cells (Fig. 3C).

Therapeutic efficacy of bevacizumab monotherapy in S-YU cell-bearing NOG mice

Photomicrographs of tumor tissue from each mouse are shown (Fig. 4A). Treatment with bevacizumab resulted in an increased percentage of tumor necrosis in the NOG/S-YU mice (mean 25.3%, median 24.1%, range 19.2–33.6%), compared to control mice (mean 15.9%, median 15.4%, range 11.7–21.0%, $P = 0.0060$) (Fig. 4B, left panel). An example of calculating the percentage necrotic area is presented in Fig. 4B, right-hand panels. Bevacizumab treatment resulted in decreased vascular number in the tumor tissues [3.1, 2.6,

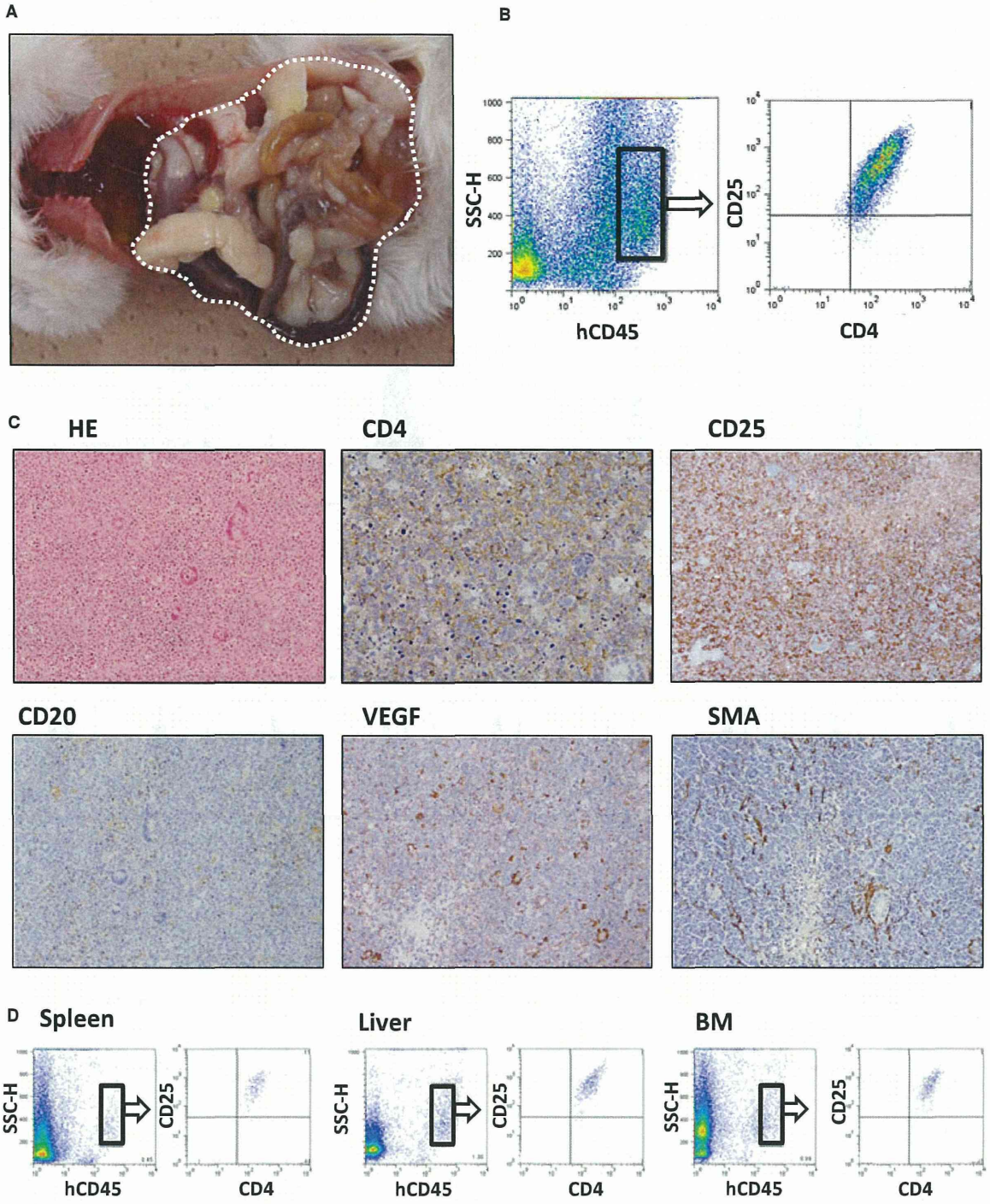

Figure 2 ATL cell-bearing NOG mouse model. (A) Macroscopic appearance of a primary DLBCL cell-bearing ATL mouse. The intraperitoneal mass is demarcated by a thin white dotted line. (B) Human CD45-positive cells in the mass determined by human CD4 and CD25 expression. (C) Immunohistochemical images of the intraperitoneal mass. (D) Human CD45-positive cells of each organ determined by human CD4 and CD25 expression.

0.0–8.3/mm^2; (mean, median, range)], compared to controls (12.8, 15.6, 1.6–19.3/mm^2, P = 0.0127) (Fig. 4C, left panel). An example of this calculation is presented in Fig. 4C, right-hand panels. Because sIL2R appears in the serum, concomitant with its increased expression on cells, we measured human sIL2R concentrations as a surrogate marker reflecting

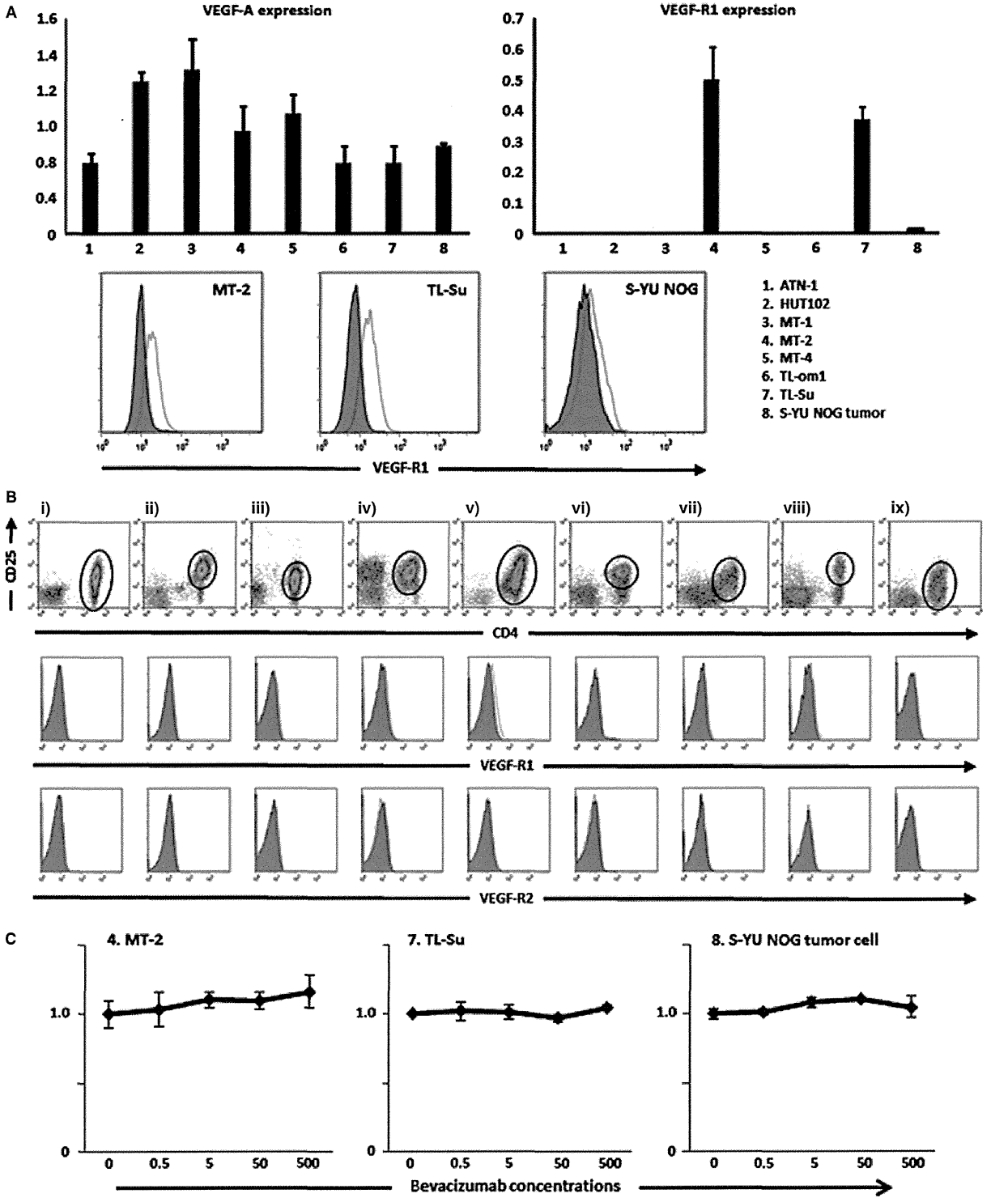

Figure 3 *Vascular endothelial growth factor A (VEGF-A), VEGF-R1, and -R2 expression in primary ATL cells, or ATL and HTLV-1-immortalized lines* (A) Quantitative RT-PCR analysis for VEGF-A and VEGF-R1 in 7 ATL and HTLV-1-immortalized lines, and NOG ATL cells from the intraperitoneal mass (upper panels). Flow cytometry for VEGF-R1 in HTLV-1-immortalized lines MT-2 and TL-Su, and NOG ATL cells, from the intraperitoneal mass (lower panels). (B) Flow cytometry for VEGF-R1, and -R2 in 9 primary ATL cells. (C) Bevacizumab has no direct anti-proliferative activity against HTLV-1-immortalized lines (MT-2 and TL-Su) expressing both VEGF-A and VEGF-R1, or NOG ATL cells, *in vitro*. Each result represents three independent experiments.